Monthly Notices of the ROYAL ASTRONOMICAL SOCIETY

MNRAS **552,** 1–13 (2026)
Advance Access publication 2026 September 22

https://doi.org/10.1093/mnras/stag1791

ExoMol line lists – LXXI. The rovibrational quadrupole spectrum of N_2

Jake Clark-Brown, Sergey N. Yurchenko and Jonathan Tennyson ★
Department of Physics and Astronomy, University College London, Gower Street, London WC1E 6BT, UK

Accepted 2026 September 14. in original form 2026 September 9

ABSTRACT

Molecular nitrogen is expected to be abundant in many planetary atmospheres, but its ground-state spectrum is intrinsically weak, making remote detection challenging. Comprehensive line lists are presented for electric quadrupole transitions within the ground electronic state of all three stable isotopologues of molecular nitrogen: $^{14}N_2$, $^{14}N^{15}N$, and $^{15}N_2$. The TRINITY line lists are generated within the ExoMol framework using the DUO nuclear-motion code from a high-accuracy direct-potential-fit potential energy curve and an *ab initio* quadrupole moment function, including Born–Oppenheimer breakdown corrections where required. Rovibrational calculations were extended to dissociation ($v \lesssim 60$) and high rotational excitation ($J \leq 80$), with high-overtone transitions affected by numerical artefacts excluded. Simulated spectra and partition functions confirm the physical consistency of the resulting line lists and demonstrate their suitability for modelling nitrogen-rich atmospheres at temperatures up to 5000 K. The TRINITY line lists are available from the ExoMol database at www.exomol.com.

Key words: molecular data – opacity – planets and satellites: atmospheres – stars: atmospheres.

1 INTRODUCTION

Molecular spectroscopy provides a powerful means of detecting and characterizing gases in planetary atmospheres and other astrophysical environments. Interpretation of observed spectra relies on molecular line lists, which catalogue the frequencies and intensities of transitions between quantized energy levels (J. Tennyson & S. N. Yurchenko 2012). Nitrogen is expected to be a major constituent of many planetary atmospheres, and its ground-state spectrum provides an important tracer of bulk composition across a wide range of temperatures. However, these transitions are intrinsically weak, making N_2 challenging to detect remotely. Existing line lists cover the strongest transitions but remain incomplete at higher excitation, limiting their applicability at elevated temperatures. As instrumental sensitivity improves, complete and reliable line lists are therefore required to support future observations of nitrogen-rich atmospheres.

Nitrogen is expected to be present across a wide range of astrophysical environments spanning several orders of magnitude in temperature. At low temperatures (∼50 K), chemical models of protoplanetary discs predict that a major nitrogen reservoir exists in the form of N_2, which remains gaseous interior to the N_2 snowline at tens of au (A.-M. A. Piso, J. Pegues & K. I. Öberg 2016). At room temperature (296 K), N_2 is the dominant constituent of Earth's atmosphere (78 per cent by volume), with 296 K adopted as the standard reference temperature in HITRAN. At higher temperatures (∼1500 K), representative of hot exoplanet atmospheres, thermochemical equilibrium calculations predict a transition in the dominant nitrogen reservoir from NH_3 to N_2 at around 600–800 K (A. Burrows & C. Sharp 1999), consistent with models of hot Jupiters (J. I. Moses 2014). At still higher temperatures (∼3000 K), relevant to ultra-hot rocky exoplanets ('lava worlds'), dayside temperatures are observationally inferred to approach 3000 K (T. G. Nguyen et al. 2020), while thermochemical calculations show that N_2 remains the dominant nitrogen-bearing species up to ∼3200 K due to its strong triple bond stability (L. Schaefer, K. Lodders & B. Fegley 2012). This temperature regime also encompasses hot brown dwarfs and late M dwarfs, suggesting that nitrogen remains chemically relevant and potentially observable in these objects.

Nitrogen is chemically stable due to its strong triple bond and is therefore expected to remain abundant across conditions ranging from cold protoplanetary environments (A.-M. A. Piso et al. 2016) to hot exoplanet atmospheres (L. Schaefer et al. 2012). Thermochemical models commonly predict N_2 to be the dominant nitrogen-bearing species in hot Jupiters and many terrestrial and super-Earth atmospheres (A. Burrows & C. Sharp 1999; Y. Miguel 2018), meaning its ground-state spectrum probes the bulk atmospheric composition rather than a minor constituent. Early studies focused primarily on ultraviolet electronic transitions observed in auroral and upper-atmospheric environments (M. H. Stevens et al. 2011, 2015). These features arise from non-thermal emission or require a far-ultraviolet source in absorption and therefore do not generally trace the bulk atmosphere. By contrast, ground-state rovibrational transitions lie in the infrared and provide a direct probe of atmospheric composition. Because N_2 has no permanent dipole moment, they occur through the much weaker electric quadrupole interaction, generally requiring long path lengths and/or high column densities for their observation.

★ E-mail: j.tennyson@ucl.ac.uk

© The Author(s) 2026.
Published by Oxford University Press on behalf of Royal Astronomical Society. This is an Open Access article distributed under the terms of the Creative Commons Attribution License (https://creativecommons.org/licenses/by/4.0/), which permits unrestricted reuse, distribution, and reproduction in any medium, provided the original work is properly cited.

Downloaded from academic.oup.com/mnras/article/552/4/stag1791/8829011 by guest on 24 October 2026

Currently, the ExoMol database hosts the WCCRMT line list for $^{14}N_2$, which only considers triplet excited states of the molecule; this is a compilation of line lists by C. M. Western et al. (2018) and E. R. Jans (2024), computed using the perturbation-theory based program PGOPHER (C. M. Western et al. 2018) in conjunction with an empirical effective Hamiltonian model based on high-level *ab initio* calculations of potential energy curves, transition moments, and spin–orbit coupling constants. The line list covers transitions within hot electronic bands $B\ ^3\Pi_g - A\ ^3\Sigma_u^+$, $B'^3\Sigma_u^- - B\ ^3\Pi_g$, $W\ ^3\Delta_u - B\ ^3\Pi_g$, and $C\ ^3\Pi_u - B\ ^3\Pi_g$, which are important in nitrogen plasmas, including lightning strikes. As the current TRINITY line lists only consider the singlet ground electronic state, they remain uncoupled to this line list.

High-quality quadrupole line lists for N_2 are available through HITRAN (I. E. Gordon et al. 2026), based on laboratory measurements and theoretical calculations that produce accurate molecular models (R. J. Le Roy, Y. Huang & C. Jary 2006; H. Li & R. J. Le Roy 2007). However, these datasets were developed primarily for terrestrial conditions, providing limited coverage of highly excited states, and not consistently treating all three stable isotopologues ($^{14}N_2$, $^{14}N^{15}N$, and $^{15}N_2$). This restricts their applicability at elevated temperatures, including those of hot exoplanet atmospheres. This work uses the same molecular framework to produce comprehensive line lists for all three isotopologues, extending coverage to higher excitation as part of the ExoMol project (J. Tennyson & S. N. Yurchenko 2012).

The theoretical framework and computational methodology used to generate and validate the line lists are described below, followed by comparison with HITRAN and an assessment of completeness at high excitation. We call these line lists TRINITY (TRI + NITrogen), as they cover all three stable isotopologues of N_2.

2 THEORY AND EXISTING WORK

A molecular line list catalogues radiative transitions between quantized molecular energy levels, providing their frequencies and intensities. The ExoMol project aims to produce comprehensive line lists for modelling and interpreting molecular spectra, particularly in exoplanet atmospheres and other hot astronomical environments, including brown dwarfs and cool stars, where highly complete datasets are required (J. Tennyson & S. N. Yurchenko 2012). Since it is generally impossible to measure every rovibrational transition experimentally, limited laboratory measurements are combined with theoretical calculations to generate complete datasets. This involves solving the nuclear-motion Schrödinger equation within the Born–Oppenheimer approximation, using an accurate potential energy curve (PEC) to determine energy levels and a corresponding molecular moment function, such as a dipole or quadrupole moment function, to determine transition intensities.

2.1 Effective potential energy curves

N_2 nuclear motion on a given PEC, $V(R)$, is governed by the Schrödinger equation

$$\left[-\frac{\hbar^2}{2\mu}\frac{d^2}{dR^2} + \frac{J(J+1)\hbar^2}{2\mu R^2} + V(R)\right]\chi_{vJ}(R) = E_{vJ}\chi_{vJ}(R), \quad (1)$$

where μ is the reduced mass, and the three terms represent vibrational kinetic energy, rotational kinetic energy, and the PEC, respectively.

Pure rotational transitions ($\Delta v = 0$) typically occur in the far-infrared, while rovibrational transitions ($\Delta v \geq 1$) lie in the infrared. For most closed-shell molecules, these arise from electric dipole radiation and obey the selection rule $\Delta J = \pm 1$. However, N_2 is homonuclear and has no permanent dipole moment, so ground-state dipole transitions are forbidden. Radiative transitions instead occur through the much weaker electric quadrupole interaction ($\Delta J = 0, \pm 2$), typically 10^6 times weaker than dipole transitions (S. Das & G. Rauhut 2026). Quadrupole transitions connect only even-J levels to even-J levels or odd-J levels to odd-J levels, producing independent para- and ortho-N_2 rotational populations.

This work adopts the recommended MLR$_4$(6, 8) potential for the ground electronic state of N_2 reported by R. J. Le Roy et al. (2006). It was obtained by fitting an analytic function directly to an extensive spectroscopic dataset comprising primarily Raman spectroscopy measurements, together with electric quadrupole rovibrational transitions and term values derived from electronic spectra.

The potential follows the Morse–long-range (MLR) form, which combines Morse-like flexibility near equilibrium with the correct asymptotic behaviour at large internuclear separation. For N_2, it is written

$$V_{\rm MLR}(R) = D_{\rm e}\left[1 - \left(\frac{R_{\rm e}}{R}\right)^n \left(\frac{1 + R_{m,n}/R^{m-n}}{1 + R_{m,n}/R_{\rm e}^{m-n}}\right) e^{-\phi(R)y_p(R)}\right]^2, \quad (2)$$

where $R_{m,n}$ are adjustable parameters, and $n = 6$ and $m = 8$ specify the inverse-power terms governing its long-range behaviour. The exponent $\phi(R)$ is expressed as a polynomial in the Šurkus radial variable

$$y_p(R) = \frac{R^p - R_e^p}{R^p + R_e^p}, \quad (3)$$

with $p = 4$. The resulting potential, along with the key parameter values, is shown in Fig. 1; the complete fitted parameters and spectroscopic dataset are given by R. J. Le Roy et al. (2006).

Prior to the study by R. J. Le Roy et al. (2006), there was no widely accepted, accurate analytic PEC for the ground state of N_2. Earlier representations, including Rydberg–Klein–Rees potentials (A. L. G. Rees 1947), reconstruct the curve pointwise from spectroscopic data and extrapolate poorly beyond the fitted region. High-quality *ab initio* calculations, such as the r12-MR-ACPF potential of R. J. Gdanitz (1998), also do not achieve full spectroscopic accuracy and show increasing discrepancies at higher vibrational levels. By contrast, the direct-potential-fit approach of R. J. Le Roy et al. (2006) reproduces the fitted spectroscopic dataset with high accuracy and is expected to provide reliable predictions for very high-J rotational levels within the range of measured vibrational levels ($v < 19$). This accuracy makes the potential well suited to calculating the rovibrational energies required for a comprehensive high-temperature line list.

Line lists are required not only for $^{14}N_2$, but also for the isotopologues $^{14}N^{15}N$ and $^{15}N_2$. Under the Born–Oppenheimer (BO) approximation the electronic PEC is independent of nuclear mass, so isotopic substitution affects the rovibrational energies only through the reduced mass in equation (1). In practice, a small isotope-dependent correction to the potential, known as the adiabatic Born–Oppenheimer breakdown (BOB) correction is required. Here we adopt the BOB term of R. J. Le Roy & Huang

Downloaded from academic.oup.com/mnras/article/552/4/stag1791/8829011 by guest on 24 October 2026

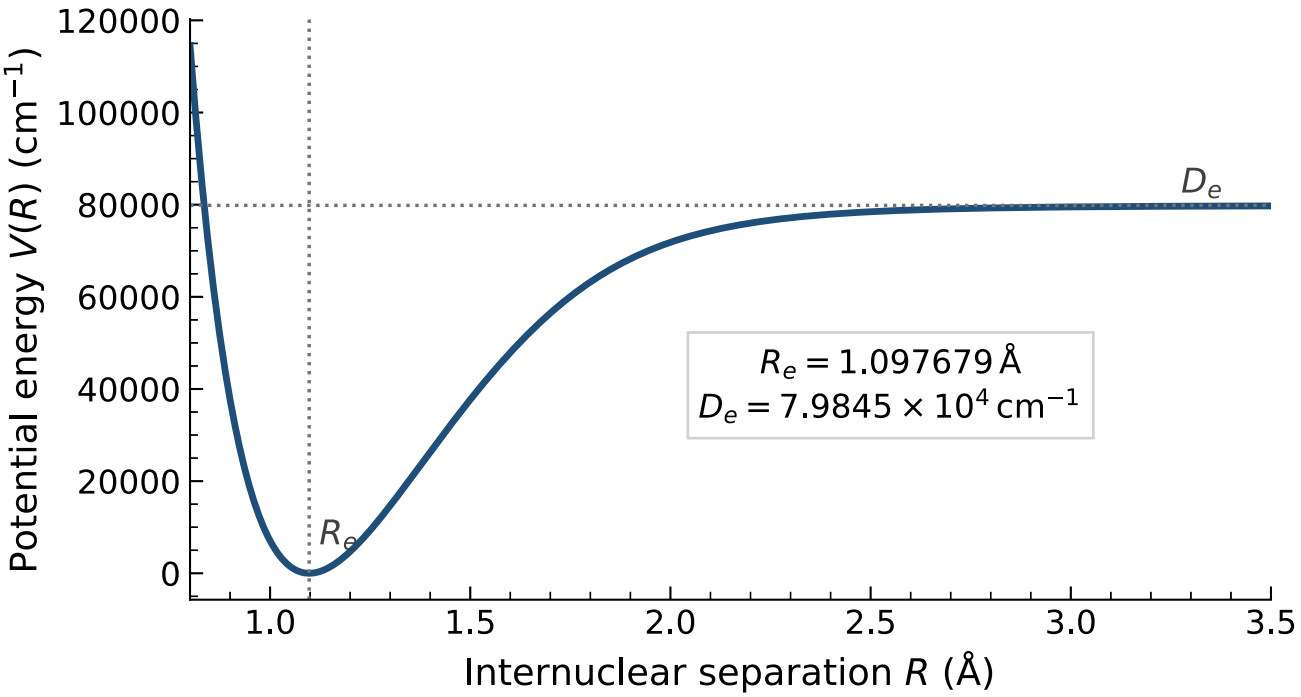


Figure 1. Potential energy curve for $^{14}N_2$ obtained from the fitted MLR$_4$(6, 8) function. The curve is shown over the range 0.8–3.5 Å; a wider grid was used in the analysis. The equilibrium bond length R_e and dissociation energy D_e are indicated.

(2002), which modifies the effective potential for isotopologue ξ as

$$V^{(\xi)}(R) = V_{\rm MLR}(R) + \Delta V_{\rm ad}^{(\xi)}(R). \quad (4)$$

The correction term is given by

$$\Delta V_{\rm ad}^{(\xi)}(R) = \left(\frac{M_{N_a}^{(\xi)} - M_{N_a}^{(1)}}{M_{N_a}^{(\xi)}} + \frac{M_{N_b}^{(\xi)} - M_{N_b}^{(1)}}{M_{N_b}^{(\xi)}} \right) S_{\rm ad}(R), \quad (5)$$

where $M_{N_{a,b}}$ are the nuclear masses and superscript (1) denotes the reference isotopologue ($^{14}N_2$). The function $S_{\rm ad}(R)$ is the adiabatic BOB radial function which, following R. J. Le Roy et al. (2006), is expressed in terms of the Surkus variable introduced above,

$$S_{\rm ad}(R) = u_1^{\rm N}\, y_6(R)\, (1 - y_6(R)), \quad (6)$$

with fitted parameter $u_1^{\rm N} = -14.1$ cm^{-1}.

The MLR potential was fitted to spectroscopic data for the reference isotopologue $^{14}N_2$ and therefore already represents its effective adiabatic potential. For other isotopologues, the isotope-dependent correction of equation (5) must be applied. R. J. Le Roy et al. (2006) tested non-adiabatic centrifugal BOB corrections, which modify the rotational kinetic-energy operator rather than the PEC, but found no discernible effect on the fit and were therefore neglected.

2.1.1 *Transition mechanisms*

In addition to electric quadrupole transitions, we considered other radiative mechanisms, but these were ultimately not included in the TRINITY line lists.

Magnetic dipole transitions: These arise from the molecular magnetic dipole moment rather than an electric multipole moment. For the ground electronic state of nitrogen ($X\,^1\Sigma_g^+$), magnetic-dipole rovibrational transitions are forbidden (Y. Chiu 1965) and are therefore not expected to contribute to the ground-state spectrum for any isotopologue.

Non-BO electric dipole transitions: Within the BO approximation, rovibrational electric dipole (E1) transitions are forbidden for N_2, including the heteronuclear isotopologue $^{14}N^{15}N$. However, the unequal nuclear masses in $^{14}N^{15}N$ slightly break this symmetry, producing a very small effective dipole moment and allowing weak E1 transitions with $\Delta J = \pm 1$. This mechanism is well established in deuterated hydrogen (HD), where purely non-BO effects give observable rovibrational transitions (K. Pachucki & J. Komasa 2008). For $^{14}N^{15}N$, the only available estimate is an early calculation by D. R. Bates (1953), giving a fundamental-band oscillator strength $f_{0\to1} \sim 2 \times 10^{-14}$. Converting this to a band-integrated absorption strength and comparing with summed quadrupole intensities gives a rough ratio $S_{\rm E1}/S_{\rm E2} \sim 3$, suggesting that non-BO E1 absorption may be comparable to or stronger than electric quadrupole (E2) absorption for this isotopologue. These transitions are not included in the HITRAN line list discussed in Section 2.3.1, and there is currently no clear observational evidence for them in either laboratory or atmospheric spectra, including the long-pathlength studies described below. Given the approximate nature of the Bates estimate and the absence of a modern dipole moment calculation, such transitions are not considered further in this work but may merit future investigation.

Collision-induced absorption (CIA): This occurs when collisions create a temporary dipole moment, allowing absorption by molecules such as N_2 that lack a permanent dipole. Unlike the discrete quadrupole spectrum, CIA forms a broad continuum that can overlap similar spectral regions. CIA scales with

Downloaded from academic.oup.com/mnras/article/552/4/stag1791/8829011 by guest on 24 October 2026

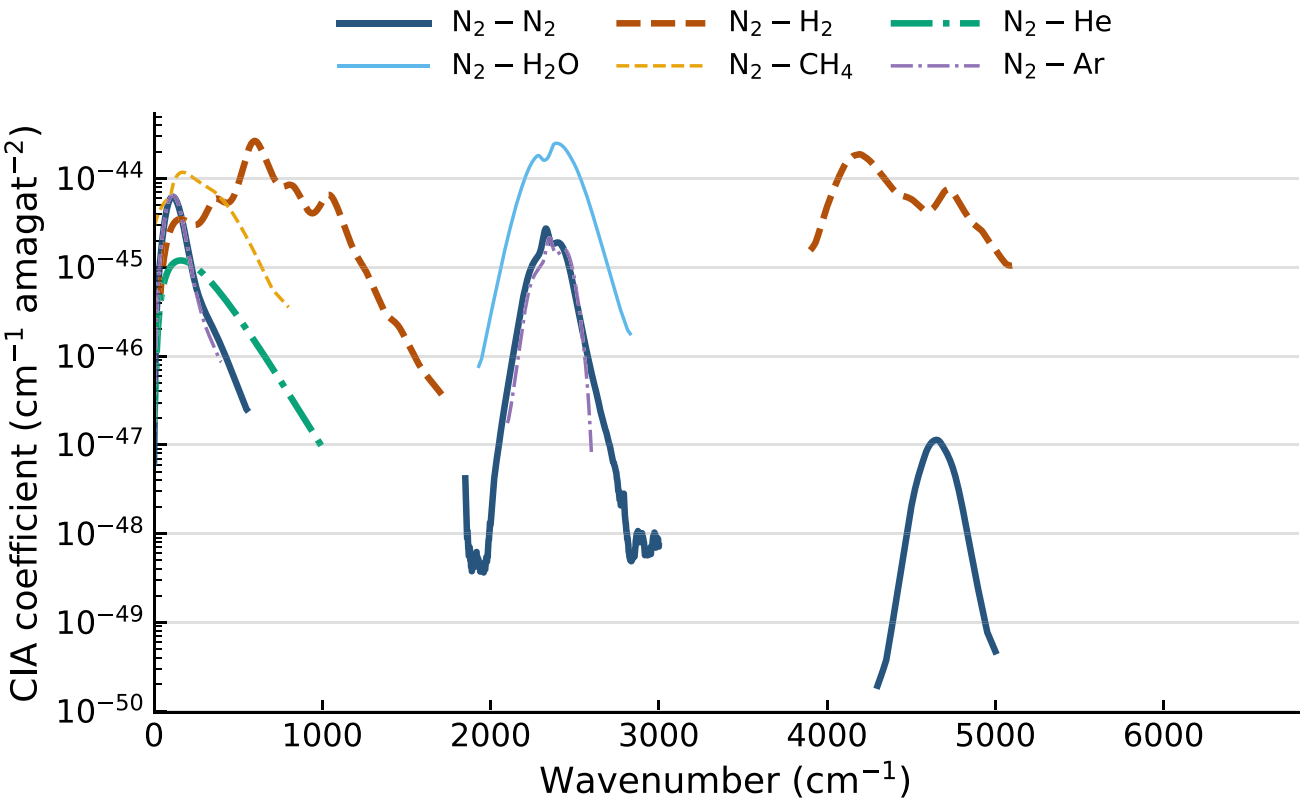


Figure 2. CIA coefficients for N_2 with selected collision partners from HITRAN (I. E. Gordon et al. 2026). The coefficient (cm^{-1} $amagat^{-2}$) gives absorption per molecular pair, where 1 amagat is the ideal-gas number density at standard conditions. Bold curves indicate the most relevant collision partners. Curves correspond to temperatures between 296 and 309.7 K (with most at 300 K), subject to data availability, and have been smoothed for clarity.

pressure squared, whereas quadrupole lines scale linearly with pressure, so CIA will become relatively more important in dense atmospheres. Fig. 2 shows representative HITRAN CIA coefficients (C. Richard et al. 2012; I. E. Gordon et al. 2026) for N_2 with several collision partners, using curves close to 296 K. Higher-temperature data are limited and available datasets are incomplete, so the figure provides qualitative guidance only; comparison with quadrupole absorption is discussed further in Section 2.3.1. We note, however, that CIA cross-sections will shortly be available via the ExoMol database.

2.2 Line intensities

While the PEC determines the rovibrational energy levels and therefore the positions of spectral lines, their intensities depend on the transition probabilities between those levels, governed by the molecular quadrupole moment function.

The strength of a spectral line is determined by the probability of radiative transitions between molecular energy levels, commonly expressed through the Einstein A coefficient that gives the spontaneous emission rate from an upper state j to a lower state i. For electric quadrupole transitions, this is given by

$$A_{ji} = \frac{64\pi^4\nu^5}{15hc^5(2J_j+1)} \left|\langle\psi_i|Q(R)|\psi_j\rangle\right|^2, \tag{7}$$

where ν is the transition frequency, J_j is the rotational quantum number of the upper state, and $Q(R)$ is the electric quadrupole moment function (QMF). The transition probability therefore depends on the matrix element of $Q(R)$ between the rovibrational wavefunctions ψ_i and ψ_j, obtained by solving equation (1). The form of the QMF therefore plays a central role in determining line intensities and constitutes the second key input required to construct the line list, alongside the PEC.

The electric quadrupole moment function, $Q(R)$, describes how the electric quadrupole moment of the molecule – a second-order moment of the charge distribution that measures its deviation from spherical symmetry – varies with internuclear separation R. The function used in this work is taken from the *ab initio* calculations of H. Li & R. J. Le Roy (2007) for the N_2 ground state. Unlike the potential energy curve, the QMF cannot generally be refined directly from experimental spectra and is therefore best obtained from *ab initio* electronic structure calculations.

The resulting QMF is shown in Fig. 3. It varies smoothly with internuclear distance R and approaches zero at large separation, as expected for two neutral atoms, and was calculated on a dense radial grid spanning 0.8–12.1a_0 (≈0.42–6.40 Å). Comparison with the PEC in Fig. 1 shows that this range fully covers the region relevant for bound rovibrational states, with increased resolution near the equilibrium separation. In this work, the tabulated values are used directly rather than fitting an analytic representation; Li & Le Roy show that spline interpolation (as used by the calculation software) converges quadrupole matrix elements to better than 10^{-6} au, so numerical effects from interpolation or limited extrapolation beyond the grid are expected to be negligible.

Downloaded from academic.oup.com/mnras/article/552/4/stag1791/8829011 by guest on 24 October 2026

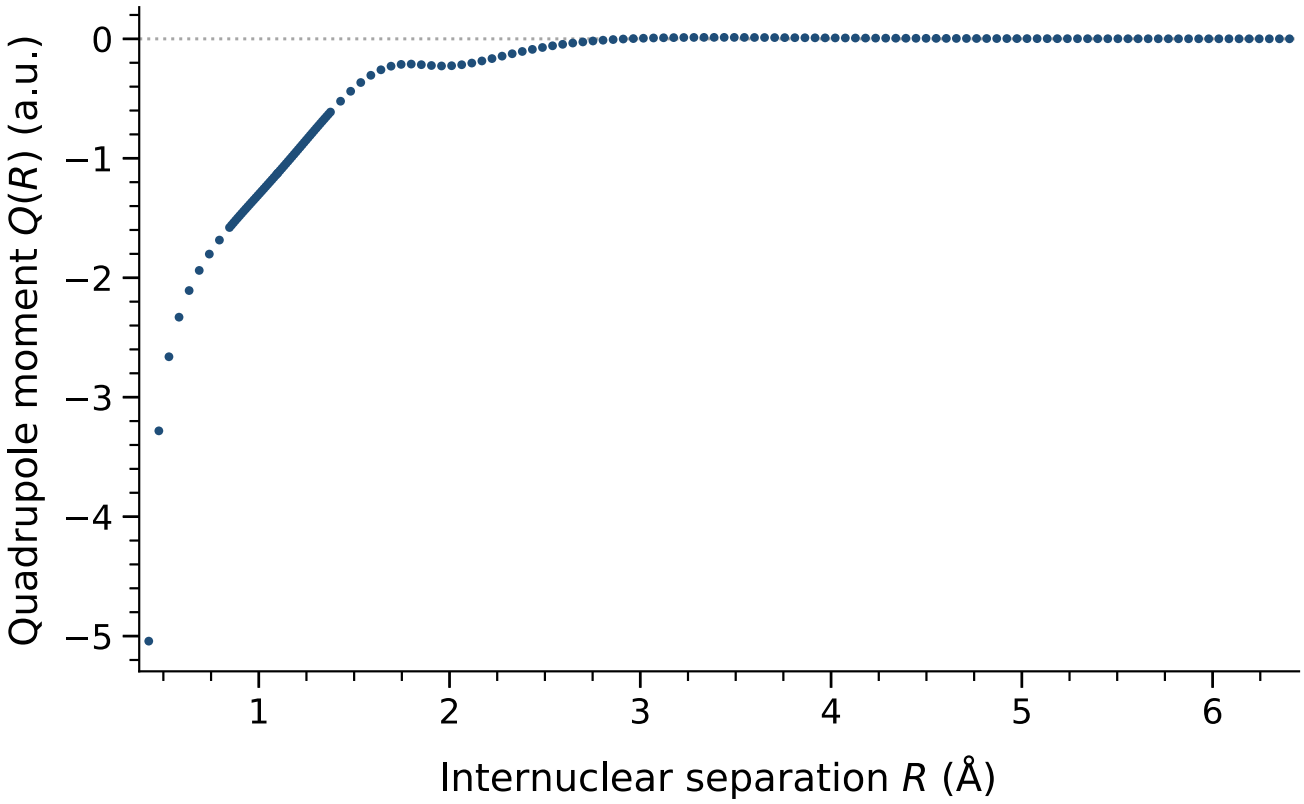


Figure 3. Analytical Li–Le Roy quadrupole moment function $Q(R)$ (in atomic units, au $= ea_0^2$) as a function of internuclear separation R. The function is sampled at 0.1 bohr, with a finer spacing of 0.02 bohr between 1.6 and 2.6 bohr.

The recommended `MR-AQCC/aug-cc-pCV5Z` model yields an equilibrium quadrupole moment $Q_e \equiv Q(R_e) = -1.1273$ au, with estimated uncertainties of approximately 0.3 per cent in Q_e and 0.8 per cent in its first radial derivative (H. Li & R. J. Le Roy 2007). Li & Le Roy show that earlier semi-empirical calculations by A. Goldman et al. (2007) underestimated quadrupole intensities by about 5 per cent. Thus, the adopted QMF provides a reliable basis for evaluating the quadrupole matrix elements $\langle v'J'|Q(R)|vJ\rangle$.

2.2.1 Key information for molecular nitrogen

Calculation of the line intensity requires knowledge of the energy level populations which depend on the partition function

$$Q(T) = \sum_i g_i e^{-E_i/kT}, \tag{8}$$

where the sum runs over the molecular energy levels E_i each with degeneracy g_i. The degeneracy is given by $g_i = g_{\rm ns}(i)(2J_i + 1)$, which is the product of the nuclear spin and rotational degeneracies. Here, $g_{\rm ns}$ is the nuclear spin statistical weight, arising from symmetry constraints on the total wavefunction. These weights determine the relative populations of even- and odd-J levels, affecting the line intensities.

Table 1 gives $g_{\rm ns}$ and other isotopologue-dependent properties of molecular nitrogen. Natural abundances I_a used in this work follow the recommended terrestrial ratio $^{14}N/^{15}N = 272$ (T. B. Coplen, H. Krouse & J. K. Böhlke 1992), consistent with HITRAN values. Molecular masses are from NIST (J. S. Coursey et al. 2015). The heteronuclear isotopologue $^{14}N^{15}N$ lacks inversion symmetry and therefore has no gerade/ungerade subscript in the term symbol.

The temperature-dependent line intensity is given by

$$S_{ij}(T) = \frac{A_{ji}}{8\pi c\tilde{\nu}_{ij}^2}\frac{g_j e^{-E_i/kT}}{Q(T)}\left(1 - e^{-hc\tilde{\nu}_{ij}/kT}\right), \tag{9}$$

where $\tilde{\nu}_{ij}$ is the transition wavenumber, and i and j denote the lower and upper states, respectively. Equation (9) links the molecular model described above to observable spectra. The PEC determines the energy levels and transition frequencies, while the QMF determines the transition matrix elements and hence the Einstein coefficients A_{ji}. Together with the partition function, these determine the line intensities, such that a line list consists of transition frequencies and Einstein A coefficients from which intensities at any temperature can be calculated. The following section presents the existing line lists for the N_2 ground state and highlights the characteristic band structure of the quadrupole spectrum.

2.3 Existing line lists and observational context

2.3.1 Existing HITRAN line lists

The HITRAN database (I. E. Gordon et al. 2026) is the standard reference source of molecular spectroscopic data, providing transition frequencies, Einstein A coefficients, line intensities, and associated quantities (like self-broadening parameters). It is regularly updated as new experimental and theoretical results become

Downloaded from academic.oup.com/mnras/article/552/4/stag1791/8829011 by guest on 24 October 2026

Table 1. Properties of the stable isotopologues of N_2.

	$^{14}N_2$	$^{14}N^{15}N$	$^{15}N_2$
Nuclear spin I	1, 1	1, $\frac{1}{2}$	$\frac{1}{2}$, $\frac{1}{2}$
Term symbol	$X\,^1\Sigma_g^+$	$X\,^1\Sigma^+$	$X\,^1\Sigma_g^+$
g_{ns} (even J)	6	6	1
g_{ns} (odd J)	3	6	3
Molecular mass (amu)	28.006	29.003	30.000
Reduced mass μ (amu)	7.000	7.241	7.500
Natural abundance I_a	$9.926\,87 \times 10^{-1}$	$7.299\,16 \times 10^{-3}$	$1.341\,76 \times 10^{-5}$

available, and is primarily designed for high-resolution modelling of radiative transfer in planetary atmospheres, particularly that of Earth. As such, the database is tabulated at a reference temperature of 296 K (approximately room temperature) and is highly reliable for terrestrial conditions, but generally lacks completeness at the higher temperatures encountered in hot exoplanet atmospheres and cool stars. At high temperatures, a far greater number of rovibrational states contribute to the spectrum, requiring more complete line lists, which is the central objective of the ExoMol project (J. Tennyson & S. N. Yurchenko 2012).

The current HITRAN line list for molecular nitrogen is based on the same underlying molecular model used in this work: the MLR_4 PEC of Le Roy et al. and the QMF of Li and Le Roy. Quadrupole transitions for $^{14}N_2$ and $^{14}N^{15}N$ were first included in HITRAN2008, with a subsequent correction to the line intensity calculations in HITRAN2012; no further updates have been made since. Transitions for $^{15}N_2$ are not avaiable from HITRAN.

The existing HITRAN line list for $^{14}N_2$ is relatively extensive at 296 K, including the fundamental band, several overtone bands, and associated hot bands, with intensities down to $\sim 10^{-39}$ cm molecule^{-1}. For higher-temperature applications, additional hot bands and higher-J states may contribute significantly. The provision is considerably more limited for $^{14}N^{15}N$, for which HITRAN only provides the fundamental band and pure rotational transitions for a reduced range of J values.

Fig. 2 shows that CIA produces a broad continuum overlapping similar spectral regions to the quadrupole bands. As CIA coefficients and line intensities are different quantities, with the CIA data not all at exactly 296 K, only a qualitative comparison is made here. In hot, high-pressure atmospheres, such as hot Jupiters, N_2–N_2 (self-CIA), N_2–H_2, and N_2–He are expected to dominate; hydrogen may obscure much of the pure rotational band and part of the first overtone, while self-CIA mainly affects the rotational region and more weakly the fundamental. Methane and water can contribute additional continuum opacity in overlapping regions, potentially complicating identification of the weakest quadrupole features.

2.3.2 *Existing observations*

Quadrupole transitions of $^{14}N_2$ have been experimentally measured, although most observations have been performed under controlled laboratory conditions due to their intrinsic weakness. No quadrupole lines have yet been measured for the minor isotopologues. The MLR_4 PEC was refined with high-precision Fourier transform spectroscopy measurements of a small number of $v = 0 \rightarrow 1$ fundamental-band transitions: 18 lines measured in the laboratory by D. Reuter, D. E. Jennings & J. W. Brault (1986) and 19 lines retrieved from aircraft-based solar occultation spectra by C. P. Rinsland et al. (1991). More recently, advances in cavity ring-down spectroscopy have enabled detection of extremely weak overtone transitions, including a first-overtone line ($v = 0 \rightarrow 2$) measured by P. Cermák et al. (2017) and two second-overtone lines ($v = 0 \rightarrow 3$) reported by S. Kassi, Gordon & Campargue (2013), with intensities on the order of 10^{-31} cm molecule^{-1}, among the weakest molecular absorption features yet measured in the laboratory. Although not included in the MLR_4 fit, good agreement of these overtone measurements with predicted line positions and intensities provides independent support for the PEC–QMF model.

Evidence that N_2 quadrupole absorption contributes measurably to atmospheric spectra has also been obtained from space-based observations. Analysis of solar occultation spectra recorded by the ACE (Atmospheric Chemistry Experiment) satellite showed that inclusion of N_2 line-by-line absorption reduces residuals in the 1900–2800 cm^{-1} region (F. Schreier et al. 2018), corresponding to the $v = 0 \rightarrow 1$ fundamental band. Individual quadrupole transitions are not resolved, but the band contribution is required to accurately reproduce the observed spectrum.

Taken together, laboratory measurements now probe extremely weak overtone transitions, supporting the PEC–QMF description in a regime not included in the original quadrupole dataset, while ACE observations show that N_2 quadrupole absorption produces a measurable band-level effect in atmospheric spectra. Existing line lists are generally sufficient given current observational capabilities, but improving instrumental sensitivity motivates extending calculations to higher vibrational and rotational excitation, particularly where isotopologue coverage remains incomplete.

3 METHODOLOGY

To obtain comprehensive rovibrational line lists for all three isotopologues of N_2, the nuclear-motion Schrödinger equation was solved using the program DUO (S. N. Yurchenko et al. 2016), a general rovibronic solver for diatomic molecules. DUO solves the one-dimensional nuclear-motion problem variationally and computes transition frequencies and Einstein A coefficients from user-specified potential energy and property curves. Since the same PEC and QMF are adopted as in HITRAN, close agreement is expected with both the HITRAN line positions and the energy levels reported by R. J. Le Roy et al. (2006), who used the program LEVEL (R. J. Le Roy 2017). Detailed comparisons between DUO and LEVEL have shown that they give very similar results with DUO capable of giving higher accuracy (I. I. Mizus et al. 2022).

3.1 Energy levels and transition frequencies

DUO supports several pre-defined analytical functional forms, and its MLR representation is equivalent to the MLR_4 form given

Downloaded from academic.oup.com/mnras/article/552/4/stag1791/8829011 by guest on 24 October 2026

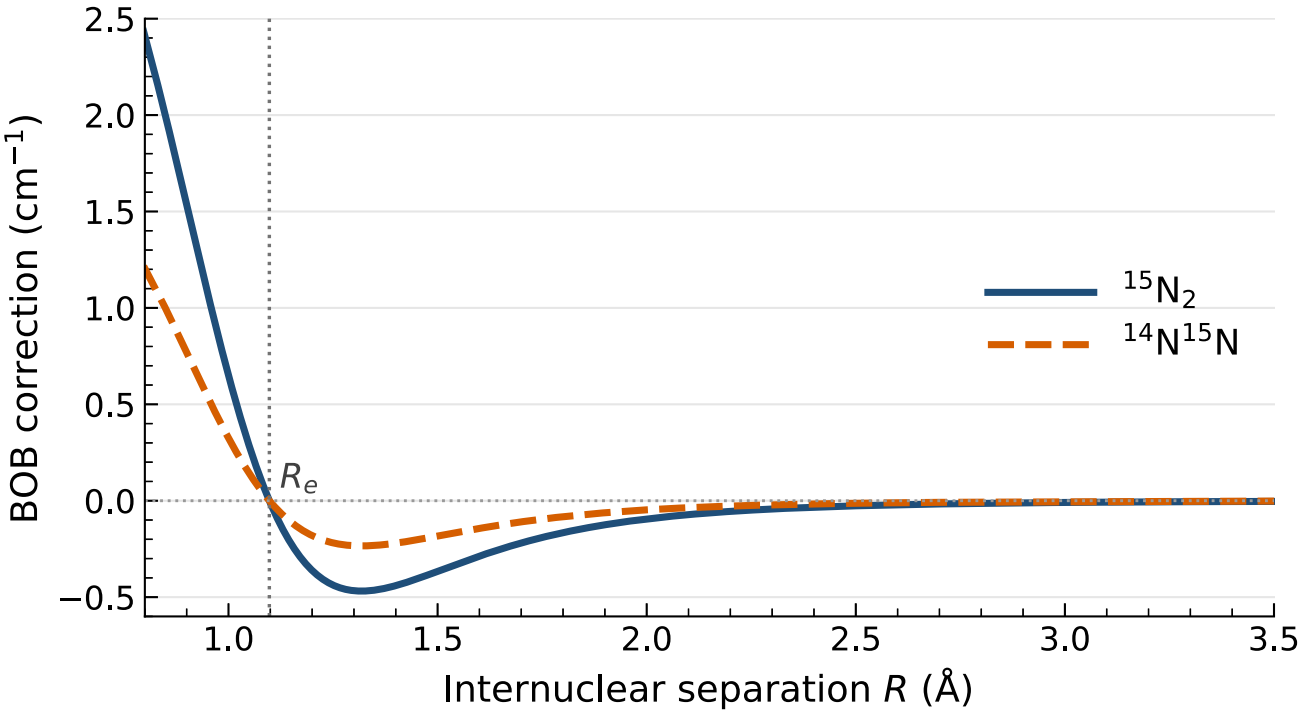


Figure 4. Adiabatic Born–Oppenheimer breakdown correction to the $^{14}N_2$ potential energy curve for $^{14}N^{15}N$ and $^{15}N_2$, shown as the difference obtained by subtracting the uncorrected Born–Oppenheimer potential from the BOB-corrected potential as a function of internuclear separation R.

in equation (2). This allows the $^{14}N_2$ potential to be implemented analytically. However, the other isotopologues require the inclusion of the adiabatic BOB correction described above, which is not currently supported analytically within DUO. The BOB-corrected PEC was therefore evaluated on a numerical grid in PYTHON and imported into DUO on the same radial grid used in the DUO calculations, avoiding interpolation. The BOB corrections are shown in Fig. 4. The correction is zero at R_e, negative at larger separations and positive at shorter separations. Since higher vibrational states sample larger average internuclear distances, the correction is expected to shift the bands considered here to lower wavenumbers. Its magnitude is of order 0.1 cm^{-1} and is therefore important for spectroscopic precision.

Calculating the PEC independently in Python introduces a small numerical discrepancy relative to DUO for numerical reasons. The relative error, of order 10^{-9}, is negligible compared to spectroscopic uncertainties and has no significant effect on calculated energy levels. Due to the discrete grid representation, the minimum of the PEC is slightly offset from zero; this is handled within DUO by disabling automatic shifting of the potential, allowing direct comparison with literature energy levels.

Energy levels were computed on linear radial grids using sinc-DVR points and a vibrational basis extending to $v_{max} = 80$. For $^{14}N_2$, 7001 points spanning $R = 0.2$–12 Å were used; for $^{14}N^{15}N$ and $^{15}N_2$, 10 001 points spanning $R = 0.2$–17 Å were used, giving nearly identical grid spacings. The lowest five vibrational levels reproduce published values to all four decimal places (R. J. Le Roy et al. 2006). The extended radial range was necessary to obtain convergence for levels approaching the dissociation energy D_e (see Fig. 1). Levels above dissociation were retained at this stage and subsequently removed during filtering (Section 3.3). States with rotational excitation up to $J = 80$ were included.

For $^{14}N_2$, all 1107 HITRAN transitions were matched and agreed to six decimal places, with residual differences of 10^{-6} cm^{-1} attributable to round-off error in the energy levels. For $^{14}N^{15}N$, all 161 HITRAN transitions were also matched, but small systematic discrepancies of order 10^{-3} cm^{-1} were observed, increasing with J. Differences are smallest for low-J rotational transitions and larger for the fundamental band. Since the computed $J = 0$ vibrational levels reproduce those of R. J. Le Roy et al. (2006) up to dissociation, the discrepancies likely originate from the HITRAN reference values, potentially reflecting a more limited basis set or omission of the BOB correction in the HITRAN calculation.

Inspection of the $^{14}N^{15}N$ HITRAN PAR file also revealed anomalously large Einstein A coefficients and identical upper- and lower-state degeneracy entries, suggesting inconsistencies in these fields. The tabulated line intensities nevertheless agree closely with those calculated here, indicating that the anomalous A coefficients were not used to generate them; the intensities were therefore retained for comparison.

Uncertainties were assigned to the calculated energy levels using a simple empirical model based on the precision and coverage of the fitted spectroscopic data (R. J. Le Roy et al. 2006). The most accurate measurements, including Raman rotational and fundamental-band spectra, have uncertainties of order 10^{-3} cm^{-1}, while hotter-band data are somewhat less precise. Since the recommended $MLR_4(6, 8)$ potential reproduces the dataset with $dd = 1.44$ (dimensionless RMS fit deviation), a baseline uncertainty of 0.002 cm^{-1} was adopted. The uncertainties were increased above $v = 7$, and more rapidly for $v > 19$, which lies beyond the experimental vibrational range included in the fit.

Downloaded from academic.oup.com/mnras/article/552/4/stag1791/8829011 by guest on 24 October 2026

Table 2. Comparison of the TRINITY line lists before and after filtering.

Isotopologue	$^{14}N_2$		$^{14}N^{15}N$		$^{15}N_2$	
	Before	After	Before	After	Before	After
Number of lines	30 462	3851	30 620	3144	31 541	1898
Max wavenumber	78 817	20 025	78 764	19 711	78 755	19 391
Max v	80	10	80	10	80	9
Max J	78	69	79	66	80	59

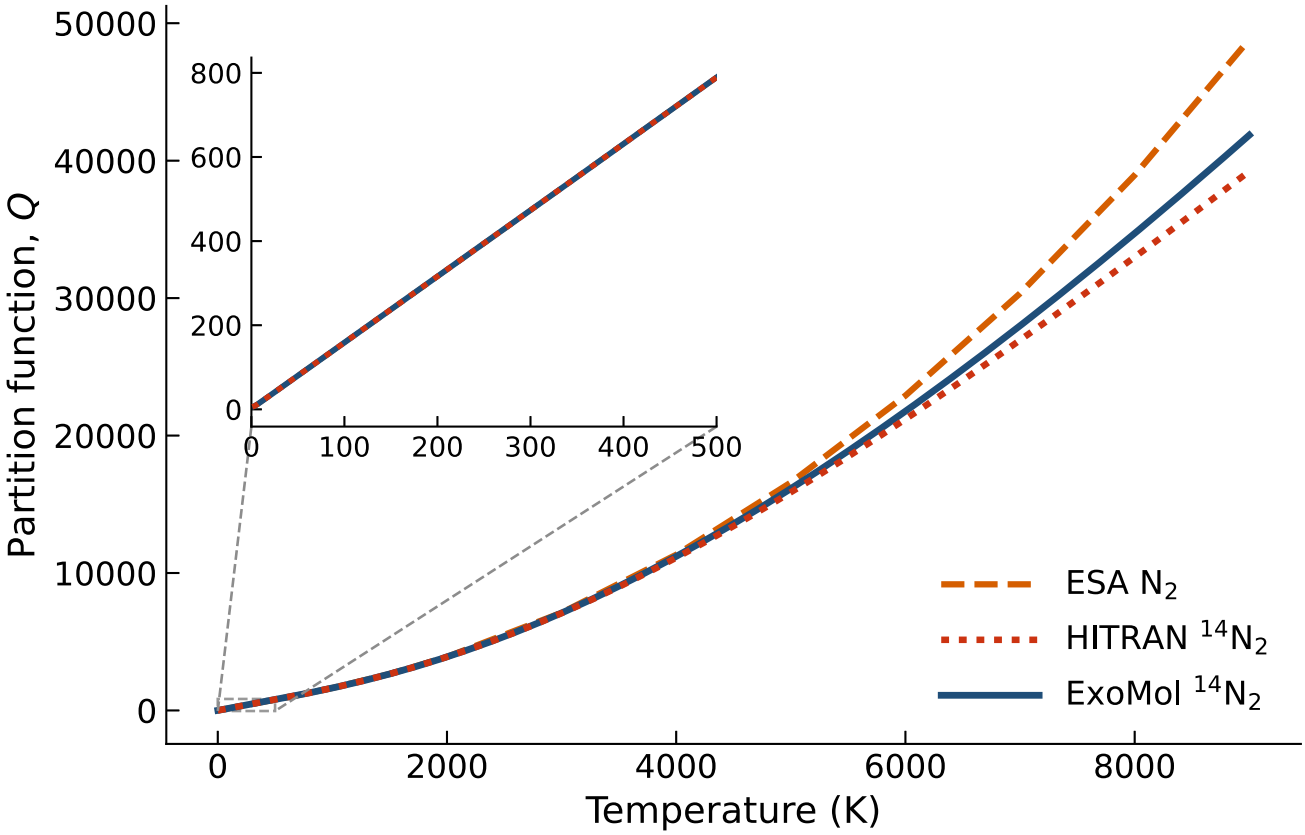


Figure 5. Comparison of the $^{14}N_2$ partition function, Q, from ESA, HITRAN, and ExoMol over 1–9000 K; the ESA values have been scaled as described in the text. The inset shows the low-temperature region from 1 to 500 K.

Table 3. Extract from the TRINITY STATES file for $^{14}N_2$.

i	E (cm^{-1})	g_i	J	Unc (cm^{-1})	τ (s)	+/−	e/f	State	v	Λ	Σ	Ω
1	0.000 000	6	0	0.000 001	Inf	+	e	$X^1\Sigma_g^+$	0	0	0	0
2	2329.911 569	6	0	0.002 000	3.9646E+07	+	e	$X^1\Sigma_g^+$	1	0	0	0
12	3.979 161	9	1	0.002 020	Inf	−	e	$X^1\Sigma_g^+$	0	0	0	0
23	11.937 345	30	2	0.002 060	1.4680E+17	+	e	$X^1\Sigma_g^+$	0	0	0	0
24	2341.744 682	30	2	0.002 060	3.9606E+07	+	e	$X^1\Sigma_g^+$	1	0	0	0
124	4889.098 608	69	11	0.003 320	1.9658E+07	−	e	$X^1\Sigma_g^+$	2	0	0	0
221	834.616 052	246	20	0.006 200	2.2514E+11	+	e	$X^1\Sigma_g^+$	0	0	0	0
222	3157.229 772	246	20	0.006 200	3.7013E+07	+	e	$X^1\Sigma_g^+$	1	0	0	0
450	22 921.504 560	486	40	0.108400	8.2905E + 11	+	e	$X^1\Sigma_g^+$	9	0	0	0
891	33 508.067 465	966	80	0.166 800	NaN	+	e	$X^1\Sigma_g^+$	10	0	0	0

Note. i: state counting number, E: state energy (cm^{-1}), g_i: total statistical weight, J: total angular momentum, Unc: uncertainty (cm^{-1}), τ: lifetime (s), Inf where the state cannot decay and NaN where the lifetime could not be computed, +/−: total parity, e/f: rotationless parity, State: electronic state, v: vibrational quantum number, Λ: projection of electronic angular momentum, Σ: projection of electron spin, and Ω: projection of total angular momentum ($\Omega = \Lambda + \Sigma$).

Downloaded from academic.oup.com/mnras/article/552/4/stag1791/8829011 by guest on 24 October 2026

Table 4. Extract from the TRINITY TRANS file for $^{14}N_2$.

i	f	A_{if} (s^{-1})	$\tilde{\nu}_{if}$ (cm^{-1})
23	1	6.8122E−18	11.937 345
34	12	1.1262E−16	19.895 115
221	199	4.4417E−12	154.847 047
2	23	2.5223E−08	2317.974 225
222	221	6.4790E−09	2322.613 719
24	23	7.4771E−09	2329.807 337
13	12	1.0469E−08	2329.876 825
24	1	5.4303E−09	2341.744 682
244	221	1.5390E−08	2491.766 881
25	1	4.0241E−10	4642.894 614

Note. i: upper state counting number, f: lower state counting number, A_{if}: Einstein A coefficient (s^{-1}), and $\tilde{\nu}_{if}$: transition wavenumber (cm^{-1}).

The fitted data extend to $J \sim 48$, and the potential is reported to remain reliable at very high J within the vibrational data range; the rotational contribution to the uncertainty was therefore kept small. A term proportional to $J(J+1)$ was included to allow a gradual increase with rotational excitation, following the functional form adopted in the ExoMol SiO line list (S. N. Yurchenko et al. 2022).

The adopted model for the uncertainty in a level energy was therefore

$$\sigma_E(v, J) = 0.002 + a\,v + bJ(J+1), \tag{10}$$

where $b = 10^{-5}\,cm^{-1}$, and

$$a = \begin{cases} 0, & v \le 7 \\ 0.01, & 7 < v \le 19 \\ 0.02, & v > 19, \end{cases} \quad (cm^{-1}).$$

The same model was applied to all isotopologues, which were derived from the same combined-isotopologue fit including BOB corrections (R. J. Le Roy et al. 2006).

3.2 Transition intensities

The quadrupole moment function (QMF) was imported into DUO on the grid shown in Fig. 3, from which Einstein A coefficients were computed. An additional factor of $\frac{\sqrt{6}}{3}$ was applied to convert the Cartesian quadrupole moment to the tensorial form used by DUO (W. Somogyi, S. N. Yurchenko & A. Yachmenev 2021). Einstein A coefficients were converted to line intensities using EXOCROSS (S. N. Yurchenko, Al-Refaie & Tennyson 2018) with natural isotopic abundances for comparison with HITRAN.

Rigorous intensity uncertainties are difficult to quantify because they depend primarily on the accuracy of the *ab initio* quadrupole moment function and its variation with molecular geometry (J. Tennyson 2012), for which limited experimental constraints exist. The QMF of Li and Le Roy is smooth and well characterized over the range of internuclear distance sampled by low-v states (see Fig. 3), supporting reliable matrix elements for the strongest transitions. Higher vibrational states probe a wider range of internuclear distance and are therefore more sensitive to the behaviour of the QMF away from equilibrium, which should lead to higher uncertainties.

Comparison with HITRAN shows strong overall agreement in transition intensities. For $^{14}N_2$, HITRAN intensities are systematically higher by approximately 0.2 per cent, while for $^{14}N^{15}N$ agreement is much closer, typically better than 0.01 per cent. These small discrepancies could be due to the numerical implementation or may reflect minor differences in partition functions (see below), but overall agreement at the sub-per cent level provides confidence in the implementation.

3.3 Validation and filtering of computed line lists

The unfiltered line lists for all three isotopologues are substantially more complete than HITRAN, containing many additional overtone and hot-band transitions extending to higher wavenumbers and lower intensities. States above the dissociation energy D_e were removed, leaving maximum vibrational quantum numbers of $v = 60$, 61, and 62 for $^{14}N_2$, $^{14}N^{15}N$, and $^{15}N_2$, respectively. The overall structure is consistent across isotopologues, as expected, with the $^{15}N_2$ line list showing similar features but at lower intensities, reflecting its lower natural abundance and confirming correct implementation.

Even below dissociation, not all calculated transitions are reliable. A consistent decrease in intensity is expected for successive overtones, but this behaviour begins to break down above approximately 20 000 cm^{-1}, indicating the onset of dominant numerical noise. Filtering is therefore required to define a physically reliable subset of the line list. The breakdown in intensity behaviour above 20 000 cm^{-1} can be understood from the expected scaling of overtone intensities. High-overtone intensities decrease approximately exponentially with increasing vibrational quantum number difference Δv, so that $\log I \propto -\Delta v$ (E. S. Medvedev 2012). This behaviour is observed up to approximately the $0 \rightarrow 9$ band, beyond which intensities flatten and scatter. Such deviations occur when transition moments become extremely small and numerical contributions become comparable to the physical matrix elements, particularly when the moment function is represented by interpolation on a grid (E. S. Medvedev et al. 2016), as is the case here. Analytical representations of the QMF can reduce these artefacts and extend the reliable overtone range (E. S. Medvedev et al. 2016), but were not explored here. Transitions with $\Delta v \ge 10$ were therefore treated as unreliable and excluded from our line lists.

A global intensity threshold of 10^{-45} cm molecule^{-1} at 296 K was also applied for all isotopologues. This lies far below foreseeable experimental sensitivity, so larger uncertainties in extremely weak transitions have negligible impact on modelling, while preserving completeness and retaining transitions that are weak at the 296 K reference temperature but may become significantly stronger at elevated temperatures.

Summary statistics for the TRINITY line lists before and after filtering are provided in Table 2.

3.4 Partition functions

The partition function provides a useful check on the completeness of the retained rovibrational energy levels, particularly for high-temperature applications where many excited states contribute. Comparison with external partition function datasets therefore helps assess whether the present line list remains sufficiently converged for high-temperature applications.

Fig. 5 compares the present results with partition functions from HITRAN and the high-temperature ESA STR-246 compilation (M. Capitelli et al. 2005) over the range 1–9000 K. The HITRAN partition functions are computed from tabulated rovibrational energy levels (R. R. Gamache et al. 2025) and are not limited by the transitions included in the HITRAN line lists. The

Downloaded from academic.oup.com/mnras/article/552/4/stag1791/8829011 by guest on 24 October 2026

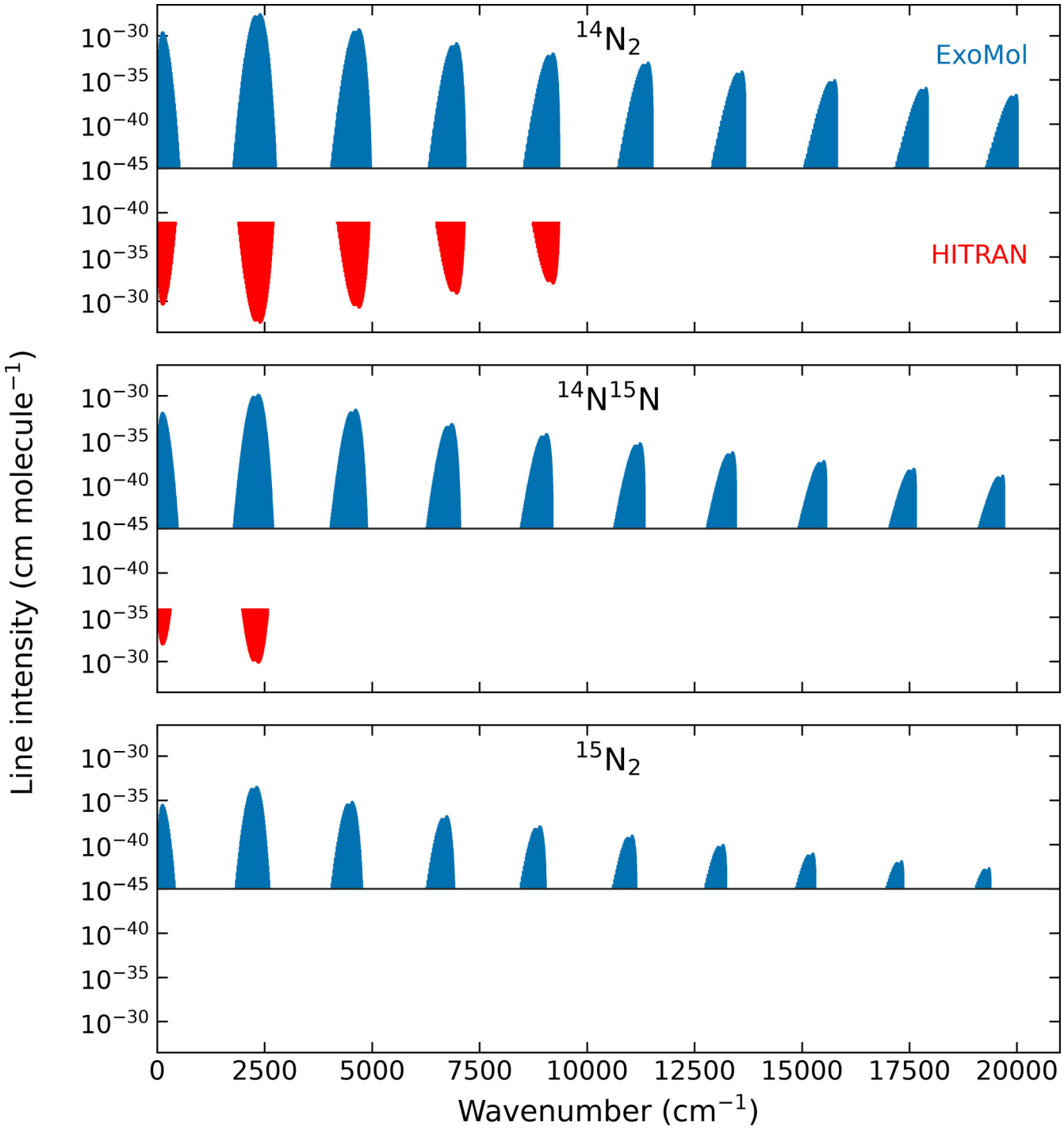


Figure 6. Mirrored stick spectra comparing the final filtered TRINITY line lists (above) with HITRAN (below) at 296 K for the three N_2 isotopologues.

Table 5. Comparison of the current HITRAN and filtered ExoMol TRINITY line lists.

Isotopologue	$^{14}N_2$		$^{14}N^{15}N$		$^{15}N_2$	
	HITRAN	ExoMol	HITRAN	ExoMol	HITRAN	ExoMol
Number of lines	1107	3851	161	3144	–	1898
Max wavenumber	9354	20025	2578	19711	–	19391
Max v	4	10	1	10	–	9
Max J	56	69	42	66	–	59

Downloaded from academic.oup.com/mnras/article/552/4/stag1791/8829011 by guest on 24 October 2026

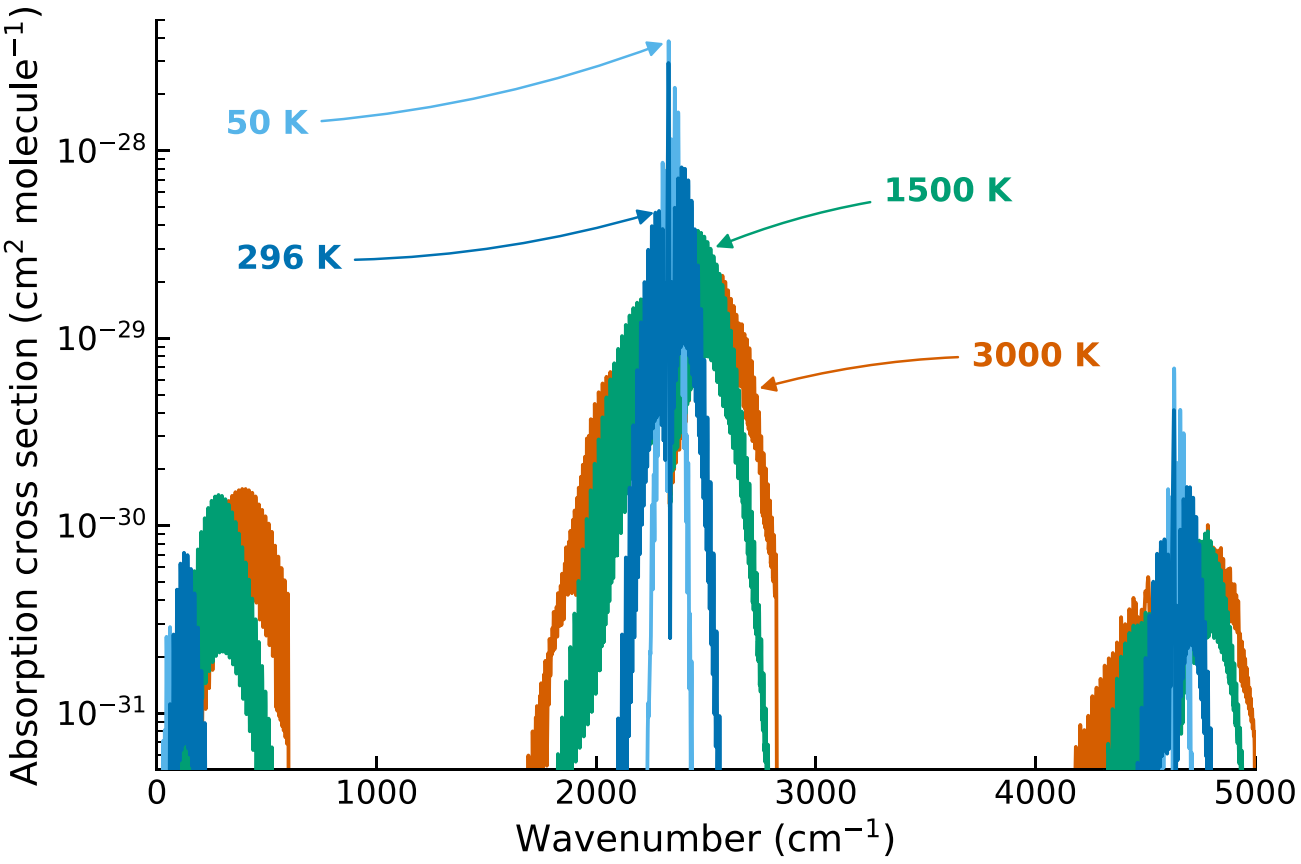


Figure 7. Simulated absorption cross-sections on a logarithmic scale for the rotational, fundamental, and first overtone bands. Contributions from all isotopologues are summed, and the spectra are Gaussian broadened with HWHM = 2 cm^{-1}. Spectra are shown for 50, 296, 1500, and 3000 K to illustrate astrophysically relevant temperature regimes.

ESA values were scaled by the nuclear spin degeneracy factor $g_{ns} = 9$ for $^{14}N_2$ to match the HITRAN/ExoMol convention. The ESA dataset includes contributions from excited electronic states and is therefore expected to exceed purely ground-state values at higher temperatures.

Excellent agreement is observed between the present results and HITRAN at low temperature, with differences of only 1.5×10^{-4} per cent at 296 K. This confirms that the small intensity discrepancies discussed above cannot be attributed to differences in the partition functions. At higher temperatures, the present partition function lies above HITRAN but below the ESA values, indicating improved convergence of the rovibrational energy level basis while remaining physically consistent with the expected electronic contributions included in STR-246. The resulting partition functions are therefore suitable for modelling high-temperature atmospheres and are provided for all three isotopologues, extending beyond the limited isotopologue coverage available in existing databases.

4 RESULTS AND DISCUSSION

The TRINITY line lists are stored in ExoMol format (J. Tennyson, C. Hill & S. N. Yurchenko 2013; J. Tennyson et al. (2024)) as a STATES file and a TRANS file, for each isotopologue; extracts are given in Tables 3 and 4. Lifetimes are computed from the complete set of Einstein *A* coefficients, before the filtering described in Section 3.3.

Fig. 6 compares the calculated TRINITY line lists with HITRAN at 296 K, showing excellent agreement for all isotopologues. All intensities match to sub-per cent accuracy, with only minor discrepancies in wavenumbers observed for $^{14}N^{15}N$. The present calculations extend substantially beyond the HITRAN coverage, both in vibrational and rotational excitation.

Table 5 summarizes the size of each line list in comparison to HITRAN. For $^{14}N_2$, the number of bands is doubled and the total number of transitions increases threefold, extending to higher *J*. For $^{14}N^{15}N$, the number of transitions increases by over an order of magnitude, with overtone and hot-band transitions included where none were previously available. A complete line list is also provided for $^{15}N_2$, for which no HITRAN data currently exist. The TRINITY line lists therefore provide substantially more complete coverage at elevated temperatures, where populations of higher-energy rovibrational states become significant.

The N_2 quadrupole spectrum varies significantly with temperature as higher rotational states and hot bands become populated. Spectra across a wide temperature range therefore help assess the need for highly excited rovibrational states in the line list, while also allowing isotopic shifts between isotopologues to be examined in high-resolution simulations. Fig. 7 shows Gaussian-broadened spectra of the first three bands at the four representative temperatures introduced in Section 1. Increasing temper-

Downloaded from academic.oup.com/mnras/article/552/4/stag1791/8829011 by guest on 24 October 2026

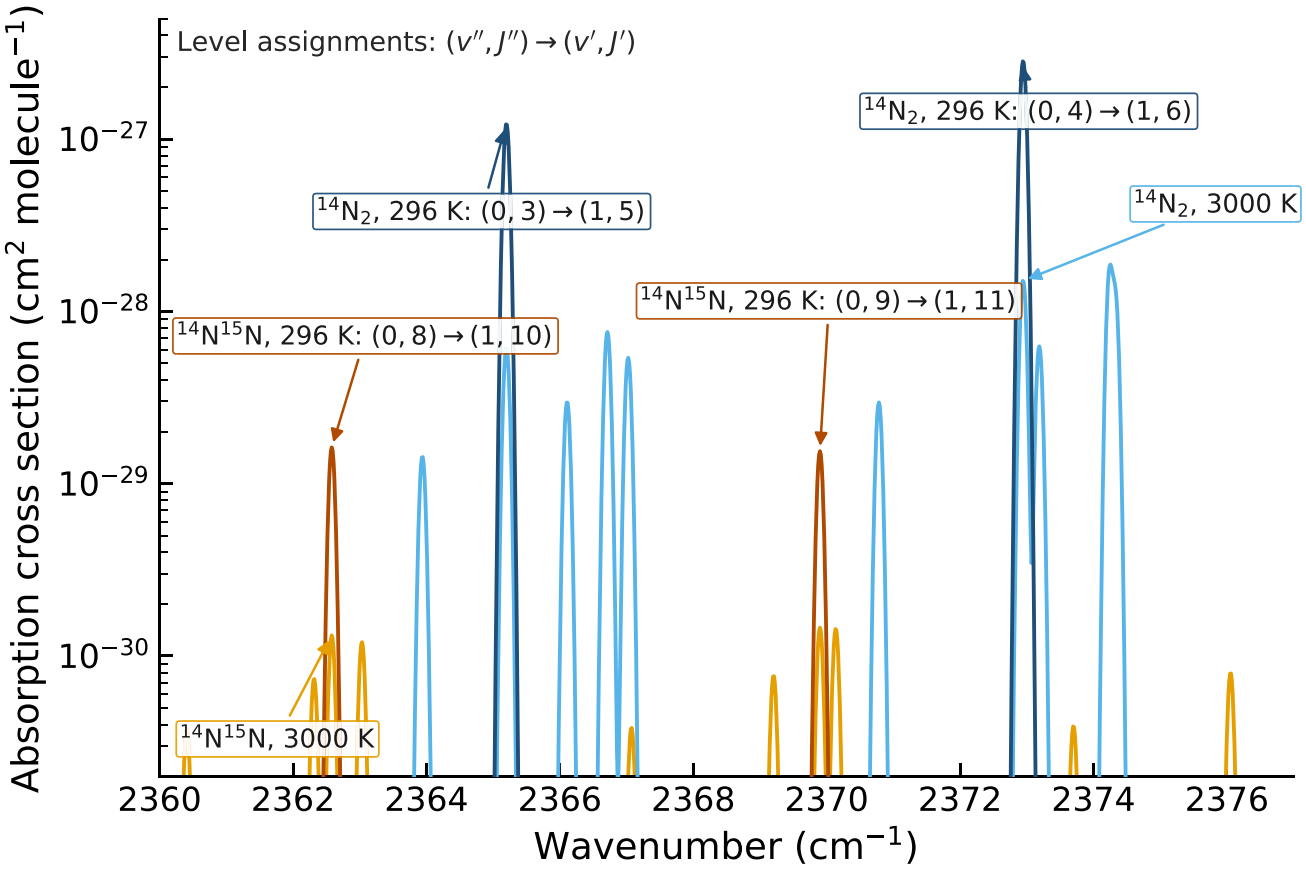


Figure 8. Simulated absorption cross-sections for $^{14}N_2$ and $^{14}N^{15}N$ in the 2360–2377 cm^{-1} region (within the fundamental band), on a logarithmic scale at 296 and 3000 K. Selected 296 K transitions are labelled using the level-assignment notation $(v'', J'') \rightarrow (v', J')$, with the corresponding 3000 K transitions indicated for comparison. The spectra were Gaussian broadened with HWHM = 0.5 cm^{-1}, with Doppler broadening neglected.

ature redistributes intensity across many transitions, producing broader and flatter band structure through population of higher rotational states and hot bands, making band features less distinct and potentially reducing detectability. The relative intensity of the fundamental and overtone bands changes little with temperature, whereas the pure rotational band becomes notably stronger and shifts to higher wavenumbers as higher-J states are populated.

Fig. 8 shows a higher-resolution view of a narrow region of the fundamental band, with isotopologue contributions shown separately. The increased hot-band contributions at higher temperatures are clearly visible, producing greater line density and a flatter spectral structure. Isotopic shifts between $^{14}N_2$ and $^{14}N^{15}N$ create distinct line positions, introducing additional spectral structure. Retrieval of isotopologue ratios would require extremely high spectral resolution and sensitivity, and is therefore expected to be challenging.

5 CONCLUSION

We present comprehensive rovibrational TRINITY line lists for electric quadrupole transitions within the ground electronic state of all three stable isotopologues of N_2: $^{14}N_2$, $^{14}N^{15}N$, and $^{15}N_2$. These line lists complement our recently complete line lists for molecular oxygen (W. Somogyi, S. N. Yurchenko & J. Tennyson 2026), which also has no dipole-allowed transitions at longer wavelengths and are available from the ExoMol website www.exomol.com.

The line lists were validated through comparison with published energy levels and existing HITRAN line lists. All 1107 HITRAN transitions for $^{14}N_2$ and 161 transitions for $^{14}N^{15}N$ were recovered. Line positions agree to within 10^{-6} cm^{-1} for $^{14}N_2$ and show small systematic differences of order 10^{-3} cm^{-1} for $^{14}N^{15}N$, increasing with J and likely reflecting limitations in the HITRAN reference calculation. Transition intensities were reproduced to sub-per cent accuracy, with typical differences of 0.2 per cent for $^{14}N_2$ and better than 0.01 per cent for $^{14}N^{15}N$, not attributable to partition function differences. Transition frequency uncertainties were estimated by extending experimental uncertainties from the fitted dataset to higher rovibrational excitation. Together, these comparisons demonstrate close overall agreement with the HITRAN line lists within the present implementation.

Simulated spectra show that hot-band and high-J transitions contribute significantly at elevated temperatures, demonstrating the need for extended rovibrational coverage when modelling environments ranging from protoplanetary discs to ultra-hot exoplanet atmospheres. Partition functions computed from the retained energy levels closely match HITRAN at low temperature and show improved convergence at high temperature, lying between HITRAN and another implementation that additionally includes excited electronic states, as expected for a purely rovi-

Downloaded from academic.oup.com/mnras/article/552/4/stag1791/8829011 by guest on 24 October 2026

brational treatment. Together, these results demonstrate that the present line lists provide a sufficiently complete description of the ground-state spectrum for high-temperature applications and are provided for all three isotopologues.

ACKNOWLEDGEMENTS

This work was supported by the European Research Council (ERC) under the European Union's Horizon 2020 research and innovation programme through Advance Grant number 883830, STFC grant UKRI/ST/B001183/1, and STFC grant ST/Y001508/1.

CONFLICT OF INTEREST

The authors declare that they have no known competing financial interests or personal relationships that could have appeared to influence the work reported in this paper.

DATA AVAILABILITY

A GitHub repository, https://github.com/jakecb123/ExoMol-N2-TRINITY, provides the DUO and EXOCROSS input and output files, together with the final ExoMol-format `.states` and `.trans` line-list files. The complete ExoMol distribution, including associated metadata files, is available via the ExoMol website, https://www.exomol.com/.

REFERENCES

Bates D. R., 1953, ApJ, 117, 236
Burrows A., Sharp C., 1999, ApJ, 512, 843
Capitelli M., Colonna G., Marraffa L., Giordano D., Warmbein B., 2005, Tables of Internal Partition Functions and Thermodynamic Properties of High-Temperature Mars-Atmosphere Species from 50 K to 50000 K. European Space Agency (European Space Research and Technology Centre, ESTEC)
Cermák P., Vasilchenko S., Mondelain D., Kassi S., Campargue A., 2017, Chem. Phys. Lett., 668, 90
Chiu Y., 1965, J. Chem. Phys., 42, 2671
Coplen T. B., Krouse H., Böhlke J. K., 1992, Pure Appl. Chem., 64, 907
Coursey J. S., Schwab D. J., Tsai J. J., Dragoset R. A., 2015, Atomic Weights and Isotopic Compositions with Relative Atomic Masses. NIST, Gaithersburg, USA, https://www.nist.gov/pml/atomic-weights-and-isotopic-compositions-relative-atomic-masses
Das S., Rauhut G., 2026, Molecular Physics, 124, e2538605
Gamache R. R., Vispoel B., Tennyson J., Yurchenko S. N., Polyansky O. L., Gordon I. E., Hargreaves R. J., Huang X., 2025, J. Quant. Spectrosc. Radiat. Transf., 345, 109568
Gdanitz R. J., 1998, Chem. Phys. Lett., 283, 253
Goldman A. et al., 2007, J. Quant. Spectrosc. Radiat. Transf., 103, 168
Gordon I. E. et al., 2026, J. Quant. Spectrosc. Radiat. Transf, 353, 109807
Jans E. R., 2024, J. Quant. Spectrosc. Radiat. Transf., 312, 108809
Kassi S., Gordon I. E., Campargue A., 2013, Chem. Phys. Lett., 582, 6
Le Roy R. J., 2017, J. Quant. Spectrosc. Radiat. Transf., 186, 167
Le Roy R. J., Huang Y., 2002, J. Mol. Struct. THEOCHEM, 591, 175
Le Roy R. J., Huang Y., Jary C., 2006, J. Chem. Phys., 125, 164310
Li H., Le Roy R. J., 2007, J. Chem. Phys., 126, 224301
Medvedev E. S., 2012, J. Chem. Phys., 137, 174307
Medvedev E. S., Meshkov V. V., Stolyarov A. V., Ushakov V. G., Gordon I. E., 2016, J. Mol. Spectrosc., 330, 36
Miguel Y., 2018, MNRAS, 482, 2893
Mizus I. I., Lodi L., Tennyson J., Zobov N. F., Polyansky O. L., 2022, J. Mol. Spectrosc., 386, 111621
Moses J. I., 2014, Phil. Trans. R. Soc. A, 372, 20130073
Nguyen T. G., Cowan N. B., Banerjee A., Moores J. E., 2020, MNRAS, 499, 4605
Pachucki K., Komasa J., 2008, Phys. Rev. A, 78, 052503
Piso A.-M. A., Pegues J., Öberg K. I., 2016, ApJ, 833, 203
Rees A. L. G., 1947, Proc. Phys. Soc., 59, 998
Reuter D., Jennings D. E., Brault J. W., 1986, J. Mol. Spectrosc., 115, 294
Richard C. et al., 2012, J. Quant. Spectrosc. Radiat. Transf., 113, 1276
Rinsland C. P., Zander R., Goldman A., Murcray F. J., Murcray D. G., Gunson M. R., Farmer C. B., 1991, J. Mol. Spectrosc., 148, 274
Schaefer L., Lodders K., Fegley B. Jr, 2012, ApJ, 755, 41
Schreier F., Städt S., Hedelt P., Godolt M., 2018, Mol. Astrophys., 11, 1
Somogyi W., Yurchenko S. N., Yachmenev A., 2021, J. Chem. Phys., 155, 214303
Somogyi W., Yurchenko S. N., Tennyson J., 2026, MNRAS, 550, stag1279
Stevens M. H. et al., 2011, J. Geophys. Res.: Space Phys., 116, A05304
Stevens M. H. et al., 2015, Geophys. Res. Lett., 42, 9050
Tennyson J., 2012, WIREs Comput. Mol. Sci., 2, 698
Tennyson J., Yurchenko S. N., 2012, MNRAS, 425, 21
Tennyson J., Hill C., Yurchenko S. N., 2013, AIP Conf. Proc. Vol. 1545. Am. Inst. Phys., New York, p. 186 10.1063/1.4815853
Tennyson J. et al., 2024, J. Quant. Spectrosc. Radiat. Transf., 326, 109083
Western C. M., Carter-Blatchford L., Crozet P., Ross A. J., Morville J., Tokaryk D. W., 2018, J. Quant. Spectrosc. Radiat. Transf., 219, 127
Yurchenko S. N. et al., 2022, MNRAS, 510, 903
Yurchenko S. N., Lodi L., Tennyson J., Stolyarov A. V., 2016, Comput. Phys. Commun., 202, 262
Yurchenko S. N., Al-Refaie A. F., Tennyson J., 2018, A&A, 614, A131

SUPPLEMENTARY MATERIAL

Supplementary data are available at *MNRAS* online.

15N2_BOB.inp
N2_analytical_PEC.inp
14N15N_BOB.inp

Please note: Oxford University Press is not responsible for the content or functionality of any supporting materials supplied by the authors. Any queries (other than missing material) should be directed to the corresponding author for the article.

This paper has been typeset from a TEX/LATEX file prepared by the author.

© The Author(s) 2026.
Published by Oxford University Press on behalf of Royal Astronomical Society. This is an Open Access article distributed under the terms of the Creative Commons Attribution License (https://creativecommons.org/licenses/by/4.0/), which permits unrestricted reuse, distribution, and reproduction in any medium, provided the original work is properly cited.

Downloaded from academic.oup.com/mnras/article/552/4/stag1791/8829011 by guest on 24 October 2026